

All-optical attoclock for imaging tunnelling wavepackets

I. Babushkin,^{1,2,3} A. J. Galan,³ J. R. C. Andrade,³ A. Husakou,³ F. Morales,³ M. Kretschmar,³ T. Nagy,³ V. Vaičaitis,⁴ L. Shi,¹ D. Zuber,^{1,2} L. Bergé,^{5,6} S. Skupin,⁷ I.A.Nikolaeva,^{8,9} N.A.Panov,^{8,9} D.E.Shipilo,^{8,9} O. G. Kosareva,^{8,9} A. N. Pfeiffer,¹⁰ A. Demircan,^{1,2,11} M. J. J. Vrakking,³ U. Morgner,^{1,2,11} and M. Ivanov³

¹*Institute for Quantum Optics, Leibniz Universität Hannover, Welfengarten 1, 30167 Hannover, Germany*

²*Cluster of Excellence PhoenixD (Photonics, Optics, and Engineering – Innovation Across Disciplines), Welfengarten 1, 30167 Hannover, Germany*

³*Max Born Institute, Max Born Str. 2a, 12489 Berlin, Germany*

⁴*Laser Research Center, Vilnius University, Saulėtekio 10, Vilnius LT-10223, Lithuania*

⁵*CEA, DAM, DIF, F-91297 Arpajon, France*

⁶*Université Paris Saclay, CEA, LMCE, 91680 Bruyères-le-Châtel, France*

⁷*Institut Lumière Matière, UMR 5306 Université Lyon 1 – CNRS, Université de Lyon, 69622 Villeurbanne, France*

⁸*Faculty of Physics, Lomonosov Moscow State University, 1 Leninskie gory, Moscow 119991, Russia*

⁹*Lebedev Physical Institute of Russian Academy of Sciences, 53 Leninskiy prospect, Moscow 119991, Russia*

¹⁰*Institute of Optics and Quantum Electronics, Abbe Center of Photonics, Friedrich Schiller University, Max-Wien-Platz 1, 07743 Jena, Germany*

¹¹*Hannover Centre for Optical Technologies, Nienburger Str. 17, 30167 Hannover, Germany*

Recent experiments on measuring time-delays during tunnelling of cold atoms through an optically created potential barrier are reinvigorating the controversial debate regarding possible time-delays during light-induced tunnelling of an electron from an atom. Compelling theoretical and experimental arguments have been put forward to advocate opposite views, confirming or refuting the existence of finite tunnelling time delays. Yet, such a delay, whether present or not, is but a single quantity characterizing the tunnelling wavepacket; the underlying dynamics are richer. Here we propose to augment photo-electron detection in laser-induced tunnelling with detection of light emitted by the tunnelling electron – the so-called Brunel radiation. Using a combination of single-color and two-color driving fields, we identify the all-optical signatures of the re-shaping of the tunnelling wavepacket as it emerges from the tunnelling barrier and moves away from the core. This reshaping includes not only an effective time-delay but also time-reversal asymmetry of the ionization process, which we describe theoretically and observe experimentally. We show how both delay and reshaping are mapped on the polarization properties of the Brunel radiation, with different harmonics behaving as different hands of a clock moving at different speeds. The all-optical detection paves the way to time-resolving optical tunnelling in condensed matter systems, e.g. tunnelling across bandgaps in solids, on the attosecond time-scale.

INTRODUCTION

Tunnelling of an electron through the potential barrier created by an oscillating electric field and the binding potential of the core is a key resource in attosecond science [1] and is at the heart of high harmonic generation and high harmonic spectroscopy [2–6]. Generally, high harmonic generation is associated with radiative recombination following the return of the laser-driven electron to the parent ion. Yet, even when the electron does not return to the core, harmonic radiation is still emitted. Often referred to as the “Brunel radiation” or “Brunel harmonics” [7–9], it is associated with bursts of current triggered by laser-induced tunnelling and is ubiquitous in atoms, molecules, and solids [10–13]. Sub-cycle tunnelling bursts occur every time the oscillating electric field goes through a maximum. Both odd and even harmonics emerge when the incident laser field contains both fundamental radiation and its second harmonic, including the so-called ‘0-th’ order Brunel harmonic corresponding to terahertz (THz) emission, see e.g. [8, 14, 15]. To produce THz radiation, the waveshape must be at least asymmetric in respect to the change $\mathbf{E} \rightarrow -\mathbf{E}$. The origin of this radiation can be traced already in a classical picture: According to Maxwell’s equations, a change of the electric current $d\mathbf{J}/dt$ produces radiation. A small volume emits, in a small time interval dt , Brunel radiation $\delta\mathbf{E}_{\text{Br}} \propto d\mathbf{J}$ produced by the change of free electron current $d\mathbf{J} \propto \rho(t)\mathbf{E}(t)dt$ due to acceleration of electrons with density $\rho(t)$ in the driving field $\mathbf{E}(t)$ in the situation when the $\rho(t)$ is time-dependent [13, 16]. Additional terms may arise due to, for instance, nonzero birth velocity of electrons (see Methods), but the above expression is rather good approximation for the lowest harmonics [17, 18].

Here we show that different Brunel harmonics generated in elliptically polarized single-color and two-color

laser fields provide a detailed picture of light-induced tunnelling. Our approach to imaging the ionization dynamics is distinctly different from the currently used attoclock approaches based on detecting photo-electrons [19–31]. It allows us to introduce a complementary, all-optical measurement protocol, which should enable one to extend measurements of tunnelling dynamics into the bulk of solids, where photo-electron spectroscopy is not readily available.

In the strong field regime, the conventional photo-electron attoclock [19, 20, 32] measures the deflection in the photo-electron spectrum generated by a few-cycle, nearly circularly polarized pulse, with respect to the pulse polarization ellipse. Interpretation of these observations uses mapping between the instant at which the electron “escapes the tunnelling barrier” and its final velocity at the detector (see Fig. 1a). This interpretation, and the possible time-delays associated with the ionization, are a subject of active discussions [25–29, 33–36], just as the general problem of tunnelling times, see e.g. the latest beautiful experiment on this subject [37]. The difficulty stems from the need to deconvolve ionization and post-ionization dynamics in the presence of the electron–core interaction, which deflects the outgoing electron and thus distorts the mapping between the tunnelling event and the measurement at a faraway detector. Moreover, possible under-the-barrier delays and the post-barrier electron velocity make the one-to-one mapping from the state at detector and emission time impossible [29, 34]. Optical techniques, relying on measuring recombination-based high harmonic emission [4, 6] instead of electron detection, face an additional challenge: the need to decouple the ionization and photo-recombination steps.

Therefore, it is advantageous to place the “observation point” as close to the tunnel exit as possible. Brunel radiation is an ideal candidate: it is produced by the current generated by the tunneling electron right near the barrier exit. We find that already the lowest, 0th-order Brunel harmonic, encodes the attosecond-scale delays and the wavepacket deflection by the core potential. The information is contained in the rotation of the polarization ellipse of this harmonic. We prove this analytically and numerically by comparing the proposed new protocol against the standard attoclock setup.

Moreover, we find theoretically and confirm experimentally that higher-order Brunel harmonics encode the temporal profile of the ionization burst, providing several connected “clock hands” rotating at different speed. Using the third-order Brunel harmonic generated in helium, we are able to reconstruct the dynamical reshaping of the electronic wavepacket during ionization. Interestingly, we find asymmetry in the ionization dynamics relative to the instantaneous peak of the driving electric field. We attribute this effect to pre- and post-ionization electron dynamics.

PHYSICAL PRINCIPLE AND THEORETICAL ANALYSIS

We first validate the key idea behind the all-optical attoclock: the vectorial properties of the emitted light, such as the rotation of the polarization ellipse, are determined by the vectorial properties of the current generated by the tunnelling electron and therefore reflect the tunnelling dynamics.

We consider two field arrangements. In the first one, intense circularly polarized infrared (IR) pump with frequency ω_0 is combined with its co-rotating second harmonic $2\omega_0$, see Fig. 1b. This generates a total electric field with one well-pronounced maximum per cycle. The orientation of this maximum, here set along the x -axis, is controlled by the relative phase between the two colors and provides the reference direction for the optical attoclock. In the second arrangement, such reference direction is provided by the major axis of the single-color elliptically polarized driving field.

All-optical measurement of strong-field ionization delays

We begin with the first arrangement. The nonlinear response contains even and odd harmonics $n\omega_0$, including the “zeroth-order” harmonic, where the signal is dominated by the Brunel radiation [38–40]. Let a classical free electron be injected by strong-field ionization into the atomic continuum with some (not necessarily zero) velocity and be accelerated in the laser field and the potential of the core. The electric field associated with the Brunel radiation, emitted by this electron, reads $\mathbf{E}_{\text{Br}}(\omega) \propto \int \frac{d\mathbf{p}(t)}{dt} e^{i\omega t} dt$, with \mathbf{p} being the electron momentum. For the 0-th harmonic $\omega \rightarrow 0$, and $\mathbf{E}_{\text{Br}}(0) \propto \mathbf{p}(t \rightarrow \infty)$. Thus, the polarization direction of the 0-th Brunel harmonic tracks the final velocity of the electron after the interaction, i.e. performs the same measurement as the photo-electron attoclock, but by all-optical means. Note that this conclusion is independent of assumptions regarding the ionization process. While exactly zero frequency cannot be observed in the experiment, measurements in the low-frequency (THz) range are feasible and discussed below.

Our conclusion also holds within the fully quantum-mechanical analysis, see Methods. In this case, $\mathbf{E}_{\text{Br}}(0)$ tracks the center of mass of the electronic wavepacket. Specifically,

$$\phi[\mathbf{E}_{\text{Br}}(0)] = \phi_\tau = \int \phi P(\phi) d\phi, \quad (1)$$

where $\phi[\mathbf{E}_{\text{Br}}(0)]$ denotes the azimuthal angle formed by the vector $\mathbf{E}_{\text{Br}}(0)$ in the xy -plane, orthogonal to the light propagation direction z , measured clockwise from the positive y direction; $P(\phi) = \int |\psi(t \rightarrow$

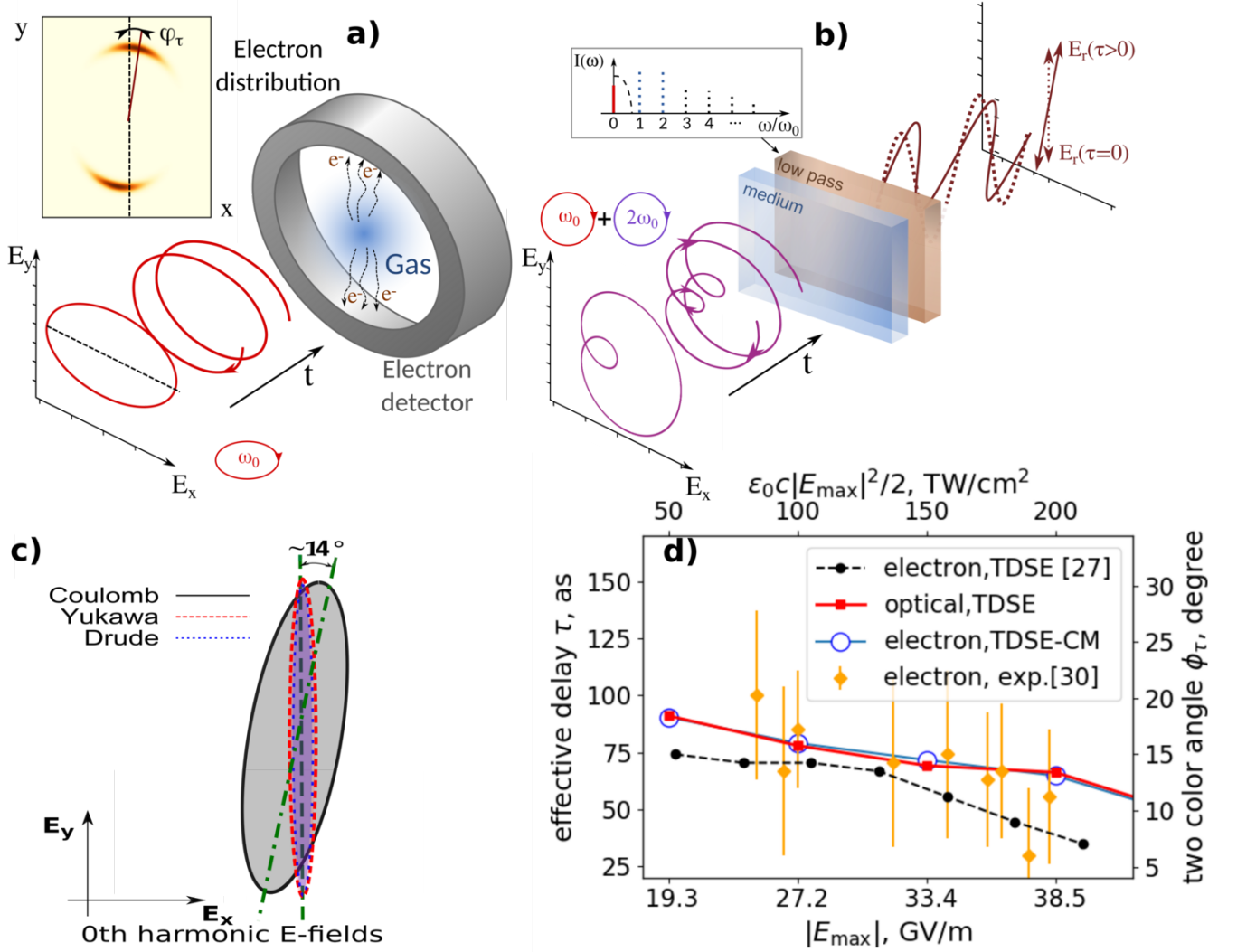


FIG. 1. Photoelectron (a) and optical (b-d) attoclock. In (a), the angle-resolved photo-electron spectrum generated by the driving field (red line) is registered at a detector, revealing attosecond delays and deflections of electronic wavepacket shifting its maximum by ϕ_τ , interpreted as an effective delay $\tau = \phi_\tau/\omega_0$. In (b), this delay is probed, instead of electrons, by the 0th-order Brunel radiation in a two-color field (magenta line). Such harmonic generated in gas or solid (blue box) can be selected by a low-pass filter (brown box). It is nearly linearly polarized (brown line) and rotated, having the same effective τ as in (a). The inset shows schematically the harmonic response spectrum, including the pump (blue) and harmonic of interest (red). (c) Polarization state of the 0th harmonic for the equivalent intensity $\epsilon_0 c |E_{\max}|^2/2 = 150 \text{ TW/cm}^2$, obtained from TDSE simulations with Yukawa potential, Coulomb potential, and using the simple-man classical Drude model. (d) Effective delay τ as a function of intensity obtained from the polarization rotation of the 0th harmonic as determined by TDSE simulations and compared to the results of the photo-electron attoclock: the center of mass position of the electronic wavepacket (TDSE-CM), as well as the simulations of [27] (where the plane $z = 0$ instead of center of masses was analyzed) and the experiment of [30].

$\infty, p, \phi, \theta)^2 p^2 \sin \theta dp d\theta$ is the photo-electron distribution integrated over the momentum and the polar angle, and $\psi(t, p, \phi, \theta)$ is the electron wavefunction in \mathbf{p} -representation. In the photo-electron attoclock, the angle ϕ_τ is mapped onto the effective ionization time-delay τ as $\phi_\tau = \omega_0 \tau$, where ω_0 is the carrier defining the "standard attoclock mapping" \mathcal{M} , $\mathcal{M}(\phi_\tau) = \phi_\tau/\omega_0 = \tau$. For our two-color field configuration, Fig. 1b, the mapping is slightly different (see Methods): $\tau = \mathcal{M}(\phi_\tau) \simeq \phi_\tau/\omega'_0$,

where $\omega'_0 = 4/3\omega_0$. This mapping should not be confused with the physical interpretation of τ , which requires the analysis of the deflection of the tunnelling electron in the core potential, possible energy gain during optical tunnelling and possibly non-zero initial electron velocity when exiting the barrier [25–29, 33–36].

Putting together Eq. (1) and the definition of \mathcal{M} for the two-color field configuration, the polarization vector

of the 0-th Brunel harmonic is predicted to be

$$\mathbf{E}_{\text{Br}}(0) \sim (\sin(\omega'_0\tau), \cos(\omega'_0\tau)), \quad (2)$$

where τ is the same effective ionization delay as obtained from the photo-electron spectrum.

We now verify this conclusion by using ab-initio time-dependent Schrödinger equation (TDSE) simulations to compute the radiated field. We start with the short-range Yukawa potential, which allows us to remove the effects of the long-range Coulomb tail of the core. In this case, the TDSE simulations show that the THz radiation is indeed nearly linearly polarized and that the major axis of its polarization ellipse is orthogonal to the major axis of the Lissajous figure of the driving two-color field, Fig. 1b,c. Thus, we confirm that, for a short-range potential supporting a single bound state, both the photo-electron attoclock and the optical attoclock measure zero ionization delays. This result also coincides with the result of classical simple-man Drude model, where Eq. (3) was used with ionization rate $\rho(t)$ calculated using Yudin-Ivanov formula [41]. The finite ellipticity seen in the TDSE results is due to the finite spectral width of the response.

For the Hydrogen atom, TDSE simulations show rotation of the polarization ellipse of the 0-th harmonic, Fig. 1c. Figure 1d compares the time-delay extracted from this rotation with the numerical results of [27] and experimental results of [30] for the photo-electron attoclock, as well as the positions of the centers of mass of the electronic wavepackets. The data points in Fig. 1d show the average polarization as discussed in Methods. This average is weighted with the spectral energy density, and coincides with the rotation angles at $\omega \rightarrow 0$ (see Supplementary). Again, we confirm that the two-color all-optical attoclock demonstrates essentially the same effective time delay τ as the single-color photo-electron one, especially if we compare the rotation angles with the center of mass of the electronic wavepacket, as our theory suggests. The broader polarization ellipse for the Coulomb potential is due to the broader spectrum of the THz response and the fact that higher frequencies are more elliptically polarized (see Supplementary).

Extending optical attoclock using higher-order Brunel harmonics

The attoclock mapping $\phi_\tau \rightarrow \tau$ establishes the relation between only two numbers, ϕ_τ and τ . We now extend the optical attoclock beyond the measurement of a single parameter to access the sub-cycle ionization yield. To this end, we consider the second field arrangement with a single-color, elliptically polarized field, see Fig. 2a, and focus on the rotation of the polarization ellipse of the higher-order Brunel harmonics.

Consider again the simple model of a classical electron extracted with zero velocity. The Brunel radiation, given

by the electrons born with ionization rate $W(t)$ and producing free current $\mathbf{J}(t)$ is described by a simple-man (so-called Drude) model [17, 42]:

$$\mathbf{E}_{\text{Br}}(t) \propto d\mathbf{J}/dt \propto \mathbf{E}(t)\rho(t) \propto \mathbf{E}(t) \int_{-\infty}^t W(t')dt', \quad (3)$$

where $\rho(t)$ is the free electron density.

On the other hand, we can also use the photo-electron spectrum and the attoclock mapping between the polar detection angle ϕ of electrons, measured at infinity, to define an effective ionization time t and ionization rate $W_e(t)$,

$$W_e(t) = P(\phi)d\phi/dt, \quad \phi = \mathcal{M}^{-1}(t). \quad (4)$$

Note that such definitions have nothing to do with the interpretation of the ionization delays in either atto-clock measurement.

As shown in the Methods section using the R-matrix approach [27, 43], the simple-man equation Eq. (4) remains fully valid also beyond the classical approximation, at least for few lowest order harmonics, if we assume $W(t) = W_e(t)$. Thus, as long as the measured harmonics are associated with the Brunel radiation, observing $\mathbf{E}_{\text{Br}}(t)$ gives all-optical access to $P(\phi)$, imaging the tunneling wavepacket by all-optical means. Below we confirm this conclusion by comparing $W(t)$ obtained optically and directly from the photo-electron distribution.

To reconstruct $W(t)$ from the Brunel radiation, we rewrite Eq. (3) in the frequency domain:

$$\mathbf{E}_{\text{Br},n} \propto \frac{i}{\omega_0} \sum_j \frac{\mathbf{E}_j W_{n-j}}{n-j}, \quad (5)$$

where W_k and \mathbf{E}_j are the Fourier components of the ionization rate and of the driving field, respectively, and $\mathbf{E}_{\text{Br},n}$ are n -th Brunel harmonics.

Already the polarization state of the 3rd harmonic gives rich information about the ionization dynamics. For the two co-rotating circular fields used above, the polarization of the 3rd harmonic is very close to circular, and thus no information can be extracted from its polarization direction since the latter is undefined. For the single-color elliptical pump (with ellipticity $\epsilon \neq 1$), see Fig. 2a, Eq (5) yields

$$\mathbf{E}_{\text{Br},3} \propto (1 + r/2, i\epsilon(1 - r/2)), \quad r = W_4/W_2. \quad (6)$$

Eq. (6) shows that the polarization state of the 3rd harmonic depends critically on the 2nd and 4th harmonics of the ionization burst $W(t)$. Most importantly, it allows us to determine whether the ionization burst is centered at the field maximum and symmetric around this center, or delayed and/or asymmetric. In the first case, the ratio $r = W_4/W_2$ is real-valued and the rotation of the polarization of the third harmonic is zero.

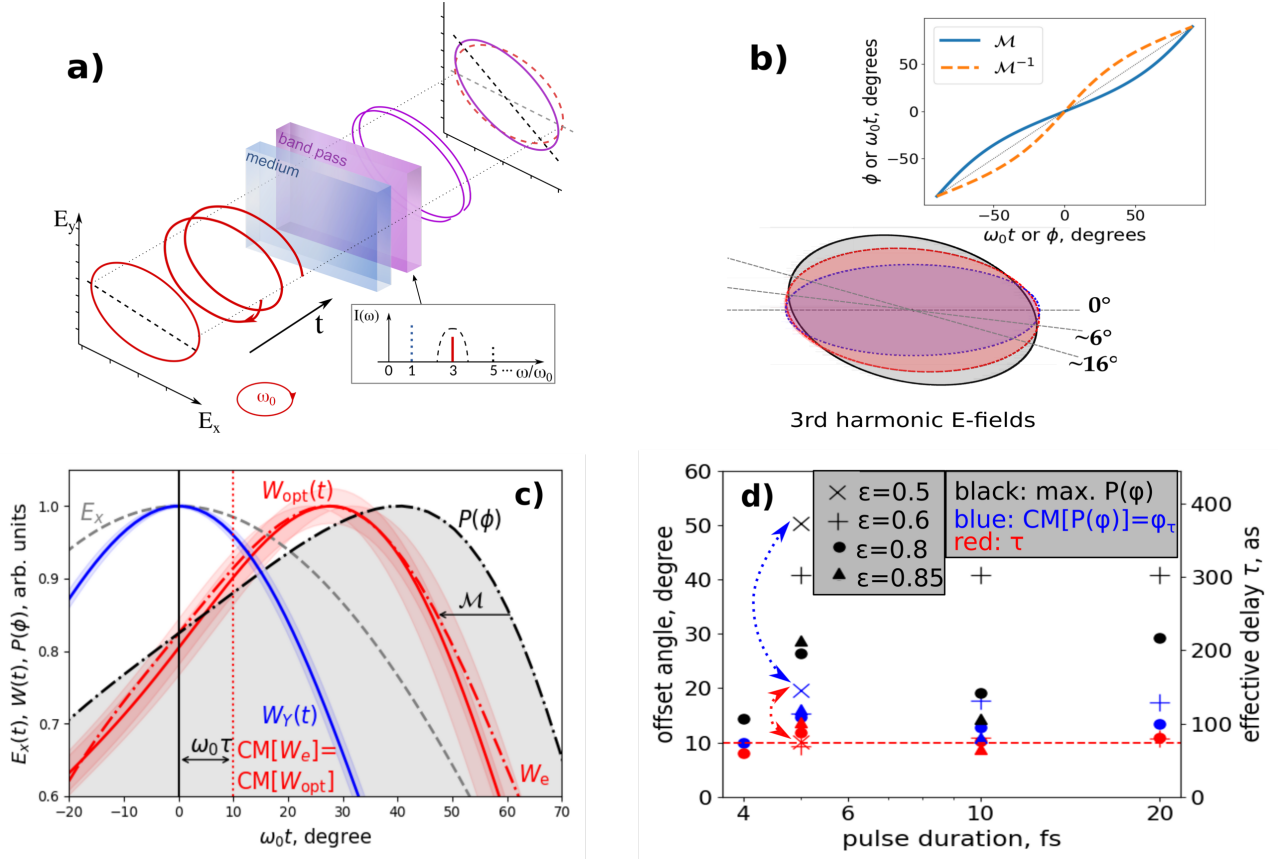


FIG. 2. Extracting photoionization information from higher order Brunel harmonics for the Hydrogen atom. In (a), a single-color elliptically polarized pump (red line) produces the 3rd Brunel harmonic (magenta line), with the polarization state (ellipticity and polarization direction) encoding the sub-cycle dynamics of the ionization process. Inset shows schematically the harmonic response spectrum, including the pump (blue) and harmonic of interest (red). (b) Polarization of the 3rd harmonic for the single-color driving pulse ($|E_{\max}| = 36.3$ GV/m, $\epsilon = 0.6$, $I = 280$ TW/cm 2) calculated using TDSE with Coulomb and Yukawa potentials as well as simple-man Drude model (denotations as in Fig. 1c). Inset shows the attoclock mapping \mathcal{M} and its inverse. (c) Optical reconstruction of the ionization dynamics ($W_{\text{opt}}(t)$, red solid line) compared to the reconstruction from the photoelectron spectrum ($W_e(t)$, red dot-dashed line) for the Coulomb potential. The estimation of error is given in Methods. Optical reconstruction for the Yukawa potential ($W_Y(t)$, blue line) is also presented. Black dot-dashed line shows the electron wavepacket distribution $P(\phi)$. The attoclock delay $\omega_0\tau$ given by the the position of the center of mass (CM) of $W_e(t) \approx W_{\text{opt}}(t)$ is also indicated (red vertical dotted line). (d) The positions of the maxima of the electronic spectra $P(\phi)$ (black markers), their CM (blue markers) and the effective delays $\tau = \mathcal{M}(\phi)$ reconstructed from the photo-electron spectra (red markers) for different FWHM pulse durations and ellipticities ϵ of the driving field. Horizontal red line shows the attoclock delay extracted optically using the two-color configuration (Fig. 1) for the corresponding peak intensity. Asymmetry of the wavepacket reveals itself from the different positions of the maximum and CM of the photo-electron spectra (see the dotted arrows tracing these for an exemplary case of $\epsilon = 0.5$).

In the second case, the ratio r is complex-valued and the polarization is rotated. Thus, extracting the phase of r from the rotation of $\mathbf{E}_{\text{Br},3}$ and comparing it with the ionization delay allows one to identify the presence of asymmetry in the ionization burst $W(t)$ with respect to its maximum. Additional information is, of course, provided by the higher-order harmonics and the phase of $r' = W_6/W_4$, $r'' = W_8/W_6$ etc. In the experiment, we focus on $\mathbf{E}_{\text{Br},3}$.

To evaluate this approach, we first make TDSE simulations for the Hydrogen atom in our single-color field configuration (Fig. 2a) and observe the polarization of the

3rd harmonic, see Fig. 2b. As expected, for the Yukawa potential the rotation of $\mathbf{E}_{\text{Br},3}$ is noticeably smaller than for the Hydrogen atom and is different from the one expected from the time-delay measured by the 0-th harmonic of the two-color optical attoclock. Together, the information extracted from both measurements is already sufficient to reconstruct $W(t)$ defined by Eq. (4) up to 4th harmonic,

$$W_{\text{opt}}(t) = W_0 + W_2 \cos(2\omega_0 t + \delta_2) + W_4 \cos(4\omega_0 t + \delta_4), \quad (7)$$

where, we changed the notations as $2|W_j| \rightarrow W_j$,

$\arg(W_j) \rightarrow \delta_j$ with respect to Eq. (5). The subscript in $W_{\text{opt}}(t)$ stresses the optical route for the reconstruction. The coefficients W_2 , W_4 , δ_2 , δ_4 are reconstructed uniquely if we assume that the center of mass of $W_{\text{opt}}(t)$ appears at $t = \tau$ (see details in Methods).

The resulting $W_{\text{opt}}(t)$ is compared in Fig. 2c with $W_e(t)$ extracted directly from the photo-electron spectra $P(\phi)$ (red solid and red dot-dashed curves, respectively). We find excellent agreement between both, proving the viability of the all-optical method.

Figure 2c shows a clear asymmetry in $W(t)$ and $P(\phi)$ with respect to time reversal, i.e., the field maximum, in the case of the Coulomb potential. This asymmetry disappears completely for the Yukawa potential, proving that the Coulomb tail not only introduces the time-delay, but also distorts the outgoing wavepacket. While in retrospect such conclusion appears transparent, hindsight is always 20/20: to the best of our knowledge, this is the first time when such asymmetry has been both reported and quantified. The presence of both non-trivial ionization phase and the distortion of the outgoing electronic wavepacket is important not only for the Brunel, but also for the recollision-based harmonics in molecules, where it will manifest as channel-dependent ionization phase associated with different ionic states between ionization and recombination, and thus different effective core potentials. Such channel-dependent ionization phase has indeed been confirmed experimentally in [44]. Interestingly, our simulations (see Fig. 2d) also show that the asymmetry becomes small for nearly circularly polarized and few-cycle pulses, suggesting that asymmetry could be also related to intermediate excitations building up inside the potential well, expected in the regime of intermediate Keldysh parameters [45]. This interpretation is further confirmed by the pronounced Freeman resonances in the rotation angle of $\mathbf{E}_{\text{Br},3}$ as a function of laser intensity; Besides, for high input intensities, saturation effects start to play a role (see Supplementary information for the case of He atom).

We note that the ionization delay τ extracted from the photo-electron spectra is nearly independent of the ellipticity and pulse duration and coincides with that extracted optically, using the two-color configuration, see Fig. 2d. We see thus that the ionization delay is, as we can judge, waveform-independent, in contrast to the deflection of the electronic cloud.

IMAGING IONIZATION DYNAMICS OF HELIUM

We now move to the experimental results. The predicted rotation of the polarization ellipse of the nonlinear response is confirmed by the experimental measurements with setup depicted in Fig. 3a. Here we report the rotation angle and the ellipticity of the third harmonic

generated by a strong pulse with ellipticity $\epsilon = 0.61$ focused in helium. The experimental approach is described in detail in the Methods section. The polarization of the pump was measured and found rotate by a negligible angle of less than 0.5 degrees upon the propagation, thus excluding the influence of plasma-induced birefringence. We note nevertheless, that the Brunel mechanism of 3rd harmonic generation competes with the $\chi^{(3)}$ -based one. Since those two mechanisms give contributions with relative phase $\pi/2$, this results in additional polarization rotation (see Supplementary Material). The correction induced by the $\chi^{(3)}$ nonlinearity is shown as a blue shaded region above the theoretical curves in Fig. 3. Its impact decreases with intensity and becomes almost negligible above $I \approx 1500 \text{ TW/cm}^2$.

The experimentally measured intensity-dependent parameters of the polarization ellipse (rotation angle and ellipticity) are shown in Fig. 3b, compared with the results of TDSE simulations for the helium atom. The details regarding the error bars are described in the Methods. Experiment and simulation are in a very good agreement. The polarization of the 3rd harmonic is rotated by nearly 5 degrees as the intensity increases from 1000 to 2000 TW/cm^2 , while the ellipticity moderately increases from around 0.56 to 0.62. Combining this information with the theoretical method developed above, we are able to reconstruct the subcycle ionization dynamics, taking the strong-field ionization delay τ of He from the experiments performed in [20].

The coefficients W_2 , W_4 , δ_2 , δ_4 , as defined in Eq. (7) and reconstructed from our measurement, are shown in Fig. 3(c,d) as a function of the pump intensity. We find that W_2 and W_4 remain nearly constant as intensity increases, whereas the angles δ_2 and δ_4 experience significant variation. The fact that W_i barely change shows that ionization remains “equally fast” for the range of intensities in the experiment. On the other hand, the growth of $|\delta_i|$ indicates the changing asymmetry of the effective sub-cycle ionization rate $W(t)$ with respect to its maximum. In Fig. 3(e,f), $W(t)$ is visualized for two values of the pump intensity, showing that the asymmetry increases with increasing intensity. While the asymmetry remains fairly small even for large intensities, its presence in the measurements is clearly seen from Fig. 3(c,d): the measured values of $|\delta_i|$ deviate substantially from zero, well beyond the experimental error bars. Thus, even small asymmetries lead to large deviations of the rotation angle, which is well detected by the all-optical method.

CONCLUSIONS AND OUTLOOK

In conclusion, we have established a firm quantitative link between measuring the photo-electron spectra in strong-field ionization and measuring the Brunel radiation generated by electrons on their way to the

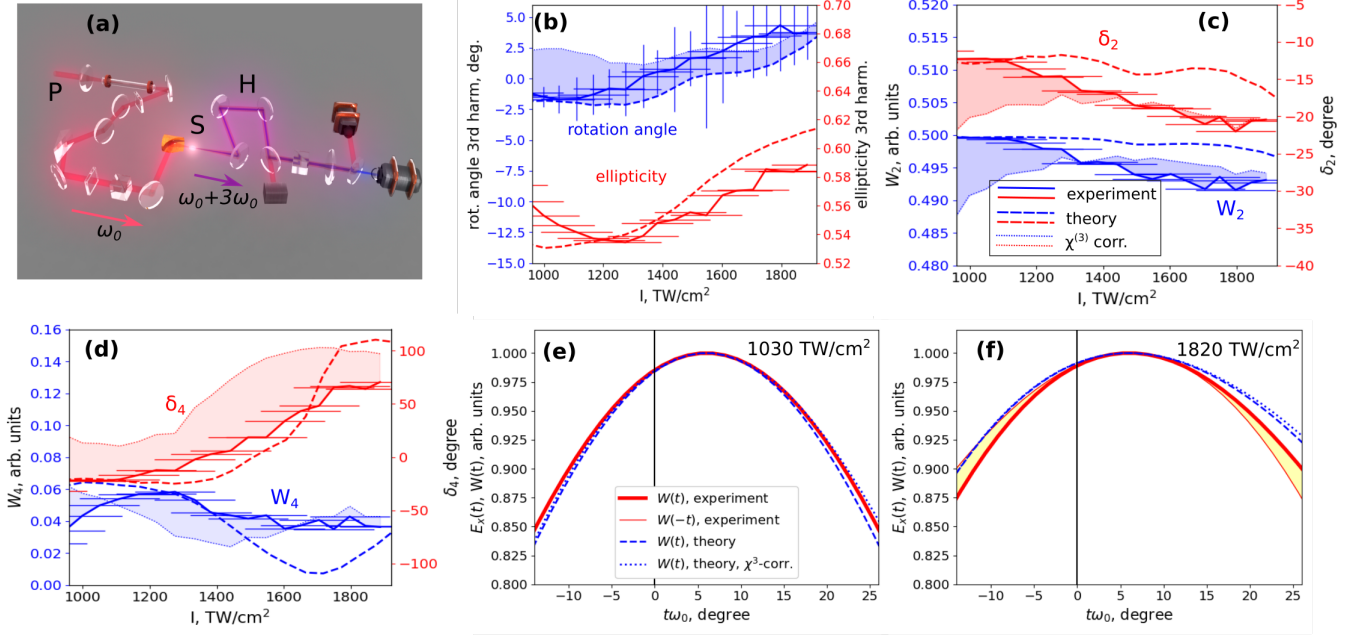


FIG. 3. Experimental reconstruction of the subcycle ionization dynamics in He, compared to the theoretical simulations. (a) Experimental setup (see Methods for more details): A 800-nm, 43-fs long elliptically-polarized pump pulse (P) is focused into a plasma spot (S) where 3rd harmonic (H) is generated. The polarization components are carefully separated and detected. (b) Experimentally measured rotation of the long axis of the 3rd harmonic with respect to the long axis of the pump (solid blue curve, left axis) and ellipticity of the 3rd harmonic (solid red curve), in comparison with the results of TDSE calculations (dashed blue and red lines). The shaded region shows uncertainty introduced by influence of bound-bound transitions. Further errors are discussed in Methods. (c),(d) Reconstruction of the coefficients W_i , δ_i describing ionization dynamics as given by Eq. (7) (with denotations as in (b)). (e),(f) Ionization dynamics $W(t)$ reconstructed for an exemplary intensities $I = 1030 \text{ TW/cm}^2$ (e) and $I = 1820 \text{ TW/cm}^2$ (f) according to experiment (thick red solid line) and theory (blue dashed line). Blue dotted line indicates the theoretical curve with bound-bound-transitions correction included. Thin red solid line indicates the time inverted $t \rightarrow -t$ version of $W(t)$ and yellow-dashed region between red lines thus indicates the asymmetry of $W(t)$ (in (e) the asymmetry is almost invisible).

continuum, revealing the reshaping of the electronic wavepacket during laser-induced tunnelling. Such reshaping is mapped on the effective ionization delays and the asymmetry of the instantaneous ionization rate with respect to the peak of the field, as it is imaged by the Brunel harmonics. According to this, Brunel harmonics in THz and UV contain signatures of attosecond- and sub-angstrom- scale electron dynamics, deeply sub-wavelength for these frequencies. Remarkably, we observe that the ionization delay is largely independent on the driving field waveshape, in contrast to the spatial reshaping of the electronic wavepacket. We attribute the origin of the ionization asymmetry to the dynamics of the electron wavepacket during and after tunnelling and, for high intensities, saturation effects. Our experiment in helium shows that the all-optical method is very sensitive even to small asymmetries of such kind. This demonstrates promising capabilities of the proposed new protocol for imaging tunnelling, which allows one to explore attosecond-scale wavepacket reshaping in systems where photo-electron detection is not readily available. One of such systems is the bulk solids, where the detection

of light is much simpler than the detection of electrons and where attosecond-scale delays were recently reported [46–48]. We foresee that Brunel harmonics of yet higher order will allow resolving electron dynamics even closer to the core.

METHODS

Experimental setup

The laser used in the experiments is a Ti:Sapphire-based regenerative amplifier (Spectra Physics Spitfire) delivering pulses with 3 mJ of energy and the spectrum supports a 43 fs of pulse duration at the driving wavelength of 800 nm. The beam was delivered to the experimental setup via an evacuated hollow-core fibre with 70% transmission. This ensured a clean beam profile with an $M^2 < 1.1$ and a 5.5 mm beam diameter. The delivered energy was selected using a pair of thin-film polarizers in combination with a broadband half-wave plate. To further attenuate the pulses and ensure the polarization purity of the electric field a fused silica wedge was used in Brewster's angle and the s-polarized pulse was used in the experiment. This allowed a tuning of the pulse energy between 40 and 225 μJ with a high linear polarization contrast. An achromatic quarter-wave plate covering the whole range of the laser spectrum was used

to convert the linear polarization into elliptical. The polarization was analyzed using a Glan-Laser calcite polarizer. The measured ellipse had an intensity ratio of 0.372 between the minor and major axes. The light was then guided into a vacuum chamber containing a parabolic gold mirror with a focal distance of 100 mm. After the focus the beam was recollimated using an Aluminium curved mirror and guided out of the chamber using further Aluminium coated mirrors. A dichroic beam-splitter was used to separate the third-harmonic from most of the fundamental. The IR light rejected by the dichroic beam splitter was directed onto a power meter in order to analyze power fluctuations during the measurements. The reflected light was used in the polarization characterization portion of the experiment. The polarization state of the third harmonic was analyzed using an α -BBO Glan-Laser polarizer (ThorLabs GLB10-UV) mounted on a home-built electronic rotation stage. Detection was performed after a dielectric HR mirror for 266 nm light allowing further separation of the UV component from the IR. The 800 nm transmitted through the 266 nm HR mirror was detected on a Silicon photodiode while the UV was measured using a Silicon Carbide (SiC) photodiode. The SiC detector is not sensitive to visible or infrared radiation, which allowed a measurement where the background is not influenced by any co-propagating IR light. All three measurement devices were connected to analogical boxcar integrators and the signals were then digitized using a 16-bit ADC connected to an arduino nano. This setup allowed to characterize the polarization state of the UV elliptical light, and to compare the direction of its long axis to that of the exciting IR field. The chamber was evacuated and subsequently filled with He at a pressure of 1.3 bar. No other nonlinearities from the optical components were observed.

Pump fields in time and frequency representation, and the attoclock mapping \mathcal{M}

We consider driving pulses propagating in z -direction, with electric field in OXY plane: $\mathbf{E} = \{E_x, E_y\}$ and vector potential $\mathbf{A}\{A_x, A_y\}$, $\mathbf{A}(t) = -\int_{-\infty}^t \mathbf{E}(t') dt'$ in the form:

$$A_x(t) = \frac{E_0}{\omega_0} e^{-2 \ln 2 t^2 / \mathcal{T}^2} \cos \omega_0 t, \quad (8)$$

$$A_y(t) = -\epsilon \frac{E_0}{\omega_0} e^{-2 \ln 2 t^2 / \mathcal{T}^2} \sin \omega_0 t, \quad (9)$$

where, in our simulations ω_0 corresponds to the carrier wavelength of 0.8 μm , E_0 is the field amplitude. The pulse duration \mathcal{T} and the ellipticity ϵ were chosen to be 20 fs and 0.61 for helium (Fig. 3). For Fig. 2c, \mathcal{T} and ϵ were 10 fs and 0.6, correspondingly. For the two-color field we have

$$A_x(t) = -\frac{E_0}{\omega_0} e^{-2 \ln 2 t^2 / \mathcal{T}^2} \left(\sin \omega_0 t + \frac{1}{2} \sin 2\omega_0 t \right), \quad (10)$$

$$A_y(t) = -\frac{E_0}{\omega_0} e^{-2 \ln 2 t^2 / \mathcal{T}^2} \left(\cos \omega_0 t + \frac{1}{2} \cos 2\omega_0 t \right), \quad (11)$$

with the same ω_0 , and $\mathcal{T} = 20$ fs.

The attoclock mapping \mathcal{M}^{-1} which maps time t to the direction of the vector potential $\mathbf{A}(t)$, that is, $\phi = \mathcal{M}^{-1}(t) \equiv \arctan(A_y(t)/A_x(t))$, with ϕ defined such that it respects the angle definition after Eq. (1), is then determined as follows: For the pulse given by Eqs. (8)-(9) we have (neglecting slow envelope effects):

$$t = \mathcal{M}(\phi) \equiv \frac{1}{\omega_0} \arctan(\epsilon \tan(\phi)). \quad (12)$$

For small ϕ can be approximated as $\mathcal{M}(\phi) \approx \phi/\omega_0'$, $\omega_0' = \omega_0/\epsilon$. For nearly circularly polarized pulses ($\epsilon \approx 1$) this expression approaches the "traditional" mapping $\tau = \mathcal{M}(\phi) = \phi/\omega_0$. Both \mathcal{M} and \mathcal{M}^{-1} are shown in the inset to Fig. 2b. For Eqs. (10)-(11), the mapping $\mathcal{M}(\phi)$ is difficult to obtain analytically, but its inverse $\mathcal{M}^{-1}(t)$ is given by:

$$\phi = \mathcal{M}^{-1}(t) \equiv \arctan \left(\frac{2 \cos(\omega_0 t) + \cos(2\omega_0 t)}{2 \sin(\omega_0 t) + \sin(2\omega_0 t)} \right), \quad (13)$$

which is rather good approximated by $\mathcal{M}^{-1}(\tau) \approx 4\omega_0\tau/3$. That is, $\tau = \mathcal{M}(\phi) \approx \phi/\omega_0'$, $\omega_0' = 4\omega_0/3$.

Jones vector formalism

In deriving the equations for the Brunel harmonics response, we used the Jones vector representation for the field harmonics $\mathbf{E}(t) = \sum_n \mathbf{E}_n e^{-in\omega_0 t}$. The waveshape described in Eqs. (8)-(11), can be easily translated into \mathbf{E}_n . For instance, a single-color field with carrier (fundamental) frequency ω_0 defined by $E_x = E_0 \cos(\omega_0 t)$, $E_y = -E_0 \sin(\omega_0 t)$ (which corresponds to the fundamental frequency component of the 2-color field) we can easily obtain using the Jones formalism as: $\mathbf{E}_1 = E_0/2 \cdot (1, -1/i)$, $\mathbf{E}_{-1} = E_0/2 \cdot (1, 1/i)$ where the first and second component of the vector are its x - and y - components, respectively. In the main text of the manuscript, the insignificant pre-factor $E_0/2$ is removed since only the polarization state matters.

TDSE simulations

The TDSE equation has the well-known form (we use atomic units here and in the following subsection):

$$i\partial_t \psi(\mathbf{r}, t) = H\psi(\mathbf{r}, t), \quad H = (\mathbf{p} + \mathbf{A}(t))^2/2 + V(r), \quad (14)$$

where $\psi(\mathbf{r}, t)$ is the wavefunction of the electron depending on space \mathbf{r} (with $r \equiv |\mathbf{r}|$) and time t , H is the electron's Hamiltonian, with \mathbf{p} being the momentum operator, $\mathbf{A}(t)$ the vector potential of the external (laser) field with the electric field strength $\mathbf{E}(t) = -\partial_t \mathbf{A}$. The simulation box size used for the integration in the two color case (Fig.1) was 500 au. In this case, to ensure the numerical convergence, simulations were repeated with both uniform and logarithmic spatial grids. For the single color case, the photo-electron spectrum (PES) in Fig. 2 was extracted by means of the iSURF method [49] using projection to Volkov states. The box size was taken to be up to 300 au in this case. The convergence of PES was also tested by projecting to the Coulomb states, obtained in a simulation with a box of 3000 au.

Reconstruction of harmonic response from the TDSE simulations

The field \mathbf{E}_r resulting from the atomic response was calculated as $\mathbf{E}_r = g\partial_{tt}\mathbf{p} = g\partial_t\mathbf{j}$, where $\mathbf{p} = \langle \psi | \mathbf{r} | \psi \rangle$ is the atomic polarization, $|\psi\rangle$ is the electron wavefunction, $\mathbf{j} = \partial_t \mathbf{p}$ is the current assigned to \mathbf{p} , and g is a constant depending on the position of the observer, which we assume equal to unity for simplicity. Note that this response contains not only Brunel but also all other nonlinearity mechanisms. For the results shown in Fig. 3, the relevant quantities (polarization direction, ellipticity) were averaged in the range $(0.75n\omega_0, 1.25n\omega_0)$ for the n th harmonic except for $n = 0$. For $n = 0$ (Fig. 1), the average was made in the range $(0, 0.25\omega_0)$, that is from zero to approx. 100 THz. In all cases, the average was performed using weighting with the intensity distribution. Examples of the spectral dependencies for 0th harmonic are shown in the Supplementary (Fig. 8).

The Drude-like model from R-matrix theory

In this section we derive the Drude-like model Eq. (5) using the framework of the analytic R-matrix approach [27, 43]. In this approach, the electron wavefunction is written as: $\psi(\mathbf{r}, t) = \sum_{t_s, \mathbf{p}} R_{\mathbf{p}} e^{iS(\mathbf{p}, t, t_s)}$ where $R_{\mathbf{p}}$ encodes the angular structure

of the initial state, t_s is a (complex-valued) stationary time (see below), and $S = S_f + S_C$, $S_f = 1/2 \int_{t_s - i\kappa}^t (\mathbf{p} + \mathbf{A}(t'))^2 dt' - I_p(t_s - t)$, $S_C = \int_{t_s - i\kappa}^t V(\mathbf{r}(\mathbf{p}, \tau, t_s)) d\tau$, where $\kappa = \sqrt{2I_p}$ and I_p is the ionization potential of the atom. The ionization time t_s is inferred via the stationary phase approach from the equation $\partial_{t_s} S = 0$. t_s is different from the ionization time t_0 in a short range potential defined from $\partial_{t_0} S_f = 0$, and hereupon we express $\tau = \text{Re}(t_s - t_0)$. According to [27], the value of τ can be obtained as a perturbation from the relation $-\tau \partial_{t_s} S_f = \partial_{t_s} S_C$. The approach of [27] can be also seen in the following way: by neglecting second and higher order derivatives of S_C as well as third and higher order derivatives of S_f , in the vicinity of t_0 we obtain $S(\mathbf{p}, t, t_s) \approx S_f(\mathbf{p}, t, t_0 + \tau) + C(t, \mathbf{p})$. That is, by changing variables $t + \tau \rightarrow t$ we transform (approximately) $S \rightarrow S_f + \text{const}(t_0)$. Here, we extend this approach, by noting that there always exists a (in general complex) function $\tau(t, \mathbf{p}, t_0)$, that makes the mapping mentioned above exact:

$$S(\mathbf{p}, t, t_s) = S_f(\mathbf{p}, t, t_0 + \tau(t, \mathbf{p}, t_0)) + C(t, \mathbf{p}) \quad (15)$$

for arbitrary t_0 . That is, introducing an effective delay τ should effectively map the Coulomb-driven dynamics after the exit of the barrier to the dynamics without the Coulomb tail. Formally speaking, this mapping is general enough to connect arbitrary functions S and S_f which are analytic everywhere except at isolated points. This leads us to the following expression for the free wavefunction

$$\psi(\mathbf{r}, t) = \sum_{t_0, \mathbf{p}} \langle \mathbf{r} | \mathbf{p} \rangle R'_\mathbf{p} e^{iS_f(\mathbf{p}, t, t_0 + \tau(t, \mathbf{p}, t_0))}, \quad (16)$$

with $R'_\mathbf{p} = R_\mathbf{p} e^{iC(t, \mathbf{p})}$. The physical meaning of τ requires that $\tau(t, \mathbf{p}, t_0) \rightarrow 0$ as $t \rightarrow t_0$, since if we consider electrons directly after the tunnel exit, they have not seen the Coulomb tail yet. On the other hand, as the modulus of $T = t - t_0$ becomes large, $\tau(t, \mathbf{p}, t - T)$ should become independent of T (meaning that at large times after the electrons were born they do not see the Coulomb tail anymore). That is, $\tau(t, \mathbf{p}, t - T)$ approaches some limiting function $\tau(t, \mathbf{p})$ at large $|T|$. In this situation, the expression for free electron density $\rho(t)$ can be most straightforwardly and transparently derived assuming a constant $C(t, \mathbf{p}) \approx C$ and only time dependent $\tau(t, \mathbf{p}) \approx \tau(t)$ at least for those \mathbf{p} which contribute mostly to Eq. (16) (see below the discussion how these assumptions can be relaxed). In this case we obtain:

$$\rho(t) = C_0 \rho_f(t - \tau(t)), \quad (17)$$

where $C_0 = e^{-2\text{Im}C}$, and $\rho_f(t)$ is the free electron density in a short range potential (that is, assuming $C = 0$, $\tau = 0$ in Eq. (16)). Neglecting $\partial_t \tau$, we also obtain that the ionization rate $W(t) \propto d\rho/dt$ which obeys the same rule: $W(t) = C_0 W_f(t - \tau(t))$, and $W_f(t)$ is the corresponding ionization rate for the short-range potential. Note that, independently from the simple derivation above, Eq. (17) provides a general transformation to map the two electron densities $\rho(t)$ and $\rho_f(t)$, except for pathological cases, if $\rho(t \rightarrow -\infty) = \rho_f(t \rightarrow -\infty) = 0$ holds. In this case, $\tau(t)$ can be calculated directly from $\rho(t)$ and $\rho_f(t)$. That means, Eq. (17) is valid also beyond the simplifications used in the derivation above. In that more general case, the expression relating the delay τ in Eq. (17) and in Eq. (15) will be more involved.

To complete the derivation of our Drude-like model, we take into account that since the mapping Eq. (15) has been applied, we have to consider electrons propagating free from the action of the Coulomb tail. Neglecting quantum interference effects in the electronic wavepacket and the term responsible for the photon absorption [12, 13, 16], we can write the current $\mathbf{J}(t)$ formed by free electrons at large enough times t as a sum of “elementary currents” from electrons born at particular times: $\mathbf{J}(t) = \int_{-\infty}^t \delta\mathbf{J}(t, t') dt'$, with $\delta\mathbf{J}(t, t') dt' = -n_0 C_0 W_f(t' - \tau(t')) (\mathbf{A}(t) - \mathbf{A}(t') + \mathbf{v}_0(t')) dt'$ represent the current from electrons born between t' and $t' + dt'$ with initial velocity \mathbf{v}_0 and atomic density n_0 . Differentiating this expression and taking into account Eq. (17), we obtain:

$$\frac{d\mathbf{J}}{dt} = n_0 (\rho(t)\mathbf{E}(t) - W(t)\mathbf{v}_0(t)). \quad (18)$$

Using the relation $d\rho \approx W(t)dt$, this expression can be reformulated as:

$$d\mathbf{J} \propto \rho(t)\mathbf{E}(t)dt - \mathbf{v}_0(t)d\rho, \quad (19)$$

which more explicitly underlines that, whereas the latter term is responsible for the birth of new electrons with nonzero velocity, the former one describes acceleration of already born electrons. The harmonics which are typically referred to as “Brunel harmonics” appear due to this former term in the situation when $\rho(t)$ is time-dependent, since if ρ is constant, the corresponding emission contains no harmonics of the driving field. According to typical analytical theories of tunneling (for instance [50]) $\mathbf{v}_0 \approx 0$, thus yielding the Drude-like model Eq.(3). We also checked that for the low frequencies considered in the present article and the values of \mathbf{v}_0 , obtained from the Wigner trajectory approach [26, 29], the term containing \mathbf{v}_0 is also negligible. A figure showing relative influence of these parameters can be found in the Supplementary. The expression Eq. (19) with $\mathbf{v}_0 = 0$ is the one shown in the Introduction.

From the expression for \mathbf{J} above, one can also see that the average propagation direction at large times is given by $\mathbf{J}_\infty = -\int C_0 W_f(t - \tau(t)) \mathbf{A}(t) dt$. That is, the number of electrons dn , born between times t and $t + dt$ flying in the direction ϕ determined by $\mathbf{A}(t)$ is given by $C_0 W_f(t - \tau(t)) dt$. At the same time by the definition of P , the same number dn is given by $P(\phi) d\phi$. Comparing these two expressions, we obtain:

$$C_0 W_f(t - \tau(t)) dt / d\phi = W(t) dt / d\phi = P(\phi), \quad (20)$$

which gives us Eq. (4), taking into account the attoclock mapping $t(\phi) = \mathcal{M}(\phi)$. In the other words: if we define a quantity $W_e(t)$ according to Eq. (4), Eq. (20) shows us that $W(t)$ defined above is identical to $W_e(t)$. That is, the effective ionization rate $W_e(t)$ obtained by mapping the angular electron spectrum into time with \mathcal{M} is equivalent to the ionization rate, we observe from the Brunel harmonics, as given by the Drude-like model Eq. (18) or Eq. (3).

As we see from the derivation above for low harmonics there is a one-to-one correspondence between wavefunction shape and the ionization rate, reflecting the effective attoclock delay τ . We see also that the delay imaged by Brunel harmonics is the same as the attoclock delay extracted from the electron distribution. This attoclock delay is also in a close connection with the Wigner delay – both are different (but closely related) measures of the group delay of the electronic wavepacket at large times. As we have seen here, if we consider τ as a function of time rather than a single number, this allows to track not only delay but also asymmetry in ionization.

As a short outlook concluding this section, for higher Brunel harmonics we can neglect neither \mathbf{v}_0 in Eq. (18), nor T -dependence in $\tau(t, \mathbf{p}, t - T)$, thus making harmonics dependent on the electron dynamics even closer to the core. This consideration is however beyond the scope of this paper.

Details of reconstruction of $W(t)$ and estimation of errors for hydrogen and helium

For the reconstruction of the W_i in Eq. (7), Fig. 2, Fig. 3 we use the following procedure: for known delay τ (which we take from [20]) and W_0 we numerically find the values of $W_2, W_4, \delta_2, \delta_4$ such that the measured value of r is achieved, and the center of mass of the reconstructed distribution is located at τ . This procedure involves numerical minimization, and gives us a unique solution for the above parameters. The value of W_0 was estimated from the ionization rate at the minimum strength of our elliptical pump field. The particular value of W_0 does not influence significantly the reconstructed dynamics. In particular, despite the analytical formula gives the symmetric ionization rate, this does not influence the asymmetry reconstructed using our procedure. We checked this with different ionization models (tunnel, ADK, Yudin-Ivanov) and obtained very similar results for the rest of W_i .

Although the observation of the 3rd harmonic provides only limited information, it is already sufficient to reconstruct the ionization dynamics with a fairly good level of precision. Indeed, we observe from our reconstruction that $|r|$ is quite small, namely $|r| = 0.14$ for the Yukawa potential and $|r| = 0.27$ for the Coulomb potential. It is reasonable to expect, that the next term in the expansion of the ionization rate is of the order of $|r|^2$ which gives us 7% uncertainty from the unknown contribution W_6 for the Coulomb potential and 2% for the Yukawa one. This determined error bars along y -axis shown in Fig. 2c. Besides, the uncertainty in δ_6 can lead to shifts along the time axis, which was taken into account by adding error bars corresponding to deviations along that axis with the amplitude equal to $|r|^2$.

In Fig. 3 the reconstruction of ionization dynamics in helium was influenced by the impact of bound-bound transitions (described in the text), errors to the experimental reconstruction were estimated using analytic signal approach discussed in Supplementary Information. In Fig. 3, the pulse energy measured in the experiment can not be directly converted to the peak intensity because of the strong influence of defocusing. We used rescaling delivered by computation of nonlinear unidirectional pulse propagation equation for $140 \mu\text{J}$, giving the peak intensity of 1000 TW/cm^2 and the waist radius $5.8 \mu\text{m}$. Still, we note that nonlinear propagation effects in the pump introduce certain uncertainty. To take this into account, we introduced intensity error bars of 10%. The details of the numerical simulations can be found in the Supplementary Information. This energy-to-intensity rescaling was used for the whole intensity range.

-
- [1] P. B. Corkum and F. Krausz, Attosecond science, *Nat. Phys.* **3**, 381 (2007).
- [2] S. Baker, J. S. Robinson, C. A. Haworth, H. Teng, R. A. Smith, C. C. Chirilă, M. Lein, J. W. G. Tisch, and J. P. Marangos, Probing proton dynamics in molecules on an attosecond time scale, *Science* **312**, 424 (2006).
- [3] O. Smirnova, Y. Mairesse, S. Patchkovskii, N. Dudovich, D. Villeneuve, P. Corkum, and M. Y. Ivanov, High harmonic interferometry of multi-electron dynamics in molecules, *Nature* **460**, 972 (2009).
- [4] B. D. Bruner, H. Soifer, D. Shafir, V. Serbinenko, O. Smirnova, and N. Dudovich, Multidimensional high harmonic spectroscopy, *J. Phys. B* **48**, 174006 (2015).
- [5] R. Torres, T. Siegel, L. Brugnera, I. Procino, J. G. Underwood, C. Altucci, R. Velotta, E. Springate, C. Froud, I. C. E. Turcu, S. Patchkovskii, M. Y. Ivanov, O. Smirnova, and J. P. Marangos, Revealing molecular structure and dynamics through high-order harmonic generation driven by mid-ir fields, *Phys. Rev. A* **81**, 051802 (2010).
- [6] O. Pedatzur, G. Orenstein, V. Serbinenko, H. Soifer, B. D. Bruner, A. J. Uzan, D. S. Brambila, A. G. Harvey, L. Torlina, F. Morales, O. Smirnova, and N. Dudovich, Attosecond tunnelling interferometry, *Nat. Phys.* **11**, 815 (2015).
- [7] F. Brunel, Harmonic generation due to plasma effects in a gas undergoing multiphoton ionization in the high-intensity limit, *J. Opt. Soc. Am. B* **7**, 521 (1990).
- [8] I. Babushkin, C. Brée, C. M. Dietrich, A. Demircan, U. Morgner, and A. Husakou, Terahertz and higher-order Brunel harmonics: from tunnel to multiphoton ionization regime in tailored fields, *J. Mod. Opt.* **64**, 1078 (2017).
- [9] T. Balciunas, A. J. Verhoef, A. V. Mitrofanov, G. Fan, E. E. Serebryannikov, M. Y. Ivanov, A. M. Zheltikov, and A. Baltuska, Optical and THz signatures of sub-cycle tunneling dynamics, *Chem. Phys.* **414**, 92 (2013).
- [10] A. A. Lanin, E. A. Stepanov, A. B. Fedotov, and A. M. Zheltikov, Mapping the electron band structure by intraband high-harmonic generation in solids, *Optica* **4**, 516 (2017).
- [11] R. E. F. Silva, Á. Jiménez-Galán, B. Amorim, O. Smirnova, and M. Ivanov, Topological strong-field physics on sub-laser-cycle timescale, *Nature Photonics* **13**, 849 (2019).
- [12] P. Jürgens, B. Liewehr, B. Kruse, C. Peltz, D. Engel, A. Husakou, T. Witting, M. Ivanov, M. J. J. Vrakking, T. Fennel, *et al.*, Origin of strong-field-induced low-order harmonic generation in amorphous quartz, *Nature Physics* **16**, 1035 (2020).
- [13] P. Jürgens, B. Liewehr, B. Kruse, C. Peltz, T. Witting, A. Husakou, A. Rouzee, M. Ivanov, T. Fennel, M. Vrakking, *et al.*, Characterization of laser-induced ionization dynamics in solid dielectrics, arXiv preprint arXiv:2108.03053 (2021).
- [14] K. Y. Kim, A. J. Taylor, J. H. Glowina, and G. Rodriguez, Coherent control of terahertz supercontinuum generation in ultrafast laser-gas interactions, *Nat. Photon.* **2**, 605 (2008).
- [15] I. Babushkin, S. Skupin, A. Husakou, C. Köhler, E. Cabrera-Granado, L. Bergé, and J. Herrmann, Tailoring terahertz radiation by controlling tunnel photoionization events in gases, *New J. Phys* **13**, 123029 (2011).
- [16] M. Geissler, G. Tempea, A. Scrinzi, M. Schnürer, F. Krausz, and T. Brabec, Light propagation in field-ionizing media: Extreme nonlinear optics, *Phys. Rev. Lett.* **83**, 2930 (1999).
- [17] I. Babushkin, S. Skupin, and J. Herrmann, Generation of terahertz radiation from ionizing two-color laser pulses in ar filled metallic hollow waveguides, *Opt. Express* **18**, 9658 (2010).
- [18] K. Zhang, K. Zhang, Y. Zhang, Y. Zhang, Y. Zhang, X. Wang, T.-M. Yan, T.-M. Yan, Y. H. Jiang, Y. H. Jiang, Y. H. Jiang, and Y. H. Jiang, Continuum electron giving birth to terahertz emission, *Photonics Research* **8**, 760 (2020).
- [19] P. Eckle, M. Smolarski, P. Schlup, J. Biegert, A. Staudte, M. Schöffler, H. G. Muller, R. Dörner, and U. Keller, Attosecond angular streaking, *Nat. Phys.* **4**, 565 (2008).
- [20] P. Eckle, A. N. Pfeiffer, C. Cirelli, A. Staudte, R. Dörner, H. G. Muller, M. Büttiker, and U. Keller, Attosecond ionization and tunneling delay time measurements in helium, *Science* **322**, 1525 (2008).
- [21] Y. Huismans, A. Rouzée, A. Gijsbertsen, J. H. Jungmann, A. S. Smolkowska, P. S. W. M. Logman, F. Lépine, C. Cauchy, S. Zamith, T. Marchenko, J. M. Bakker, G. Berden, B. Redlich, A. F. G. van der Meer, H. G. Muller, W. Vermin, K. J. Schafer, M. Spanner, M. Y. Ivanov, O. Smirnova, D. Bauer, S. V. Popruzhenko, and M. J. J. Vrakking, Time-resolved holography with photoelectrons, *Science* **331**, 61 (2011).
- [22] D. Shafir, H. Soifer, B. D. Bruner, M. Dagan, Y. Mairesse, S. Patchkovskii, M. Y. Ivanov, O. Smirnova, and N. Dudovich, Resolving the time when an electron exits a tunnelling barrier, *Nature* **485**, 343 (2012).
- [23] R. Kienberger, E. Goulielmakis, M. Uiberacker, A. Baltuska, V. Yakovlev, F. Bammer, A. Scrinzi, T. Westerwalbesloh, U. Kleineberg, U. Heinzmann, *et al.*, Atomic transient recorder, *Nature* **427**, 817 (2004).
- [24] A. N. Pfeiffer, C. Cirelli, M. Smolarski, D. Dimitrovski, M. Abu-samha, L. B. Madsen, and U. Keller, Attoclock reveals natural coordinates of the laser-induced tunnelling current flow in atoms, *Nat. Phys.* **8**, 76 (2011).
- [25] A. S. Landsman, M. Weger, J. Maurer, R. Boge, A. Ludwig, S. Heuser, C. Cirelli, L. Gallmann, and U. Keller, Ultrafast resolution of tunneling delay time, *Optica* **1**, 343 (2014).
- [26] E. Yakaboylu, M. Klaiber, and K. Z. Hatsagortsyan, Wigner time delay for tunneling ionization via the electron propagator, *Phys. Rev. A* **90**, 012116 (2014).
- [27] L. Torlina, F. Morales, J. Kaushal, I. Ivanov, A. Kheifets, A. Zielinski, A. Scrinzi, H. G. Muller, S. Sukiasyan, M. Ivanov, *et al.*, Interpreting attoclock measurements of tunnelling times, *Nat. Phys.* **11**, 503 (2015).
- [28] H. Ni, U. Saalman, and J.-M. Rost, Tunneling ionization time resolved by backpropagation, *Phys. Rev. Lett.* **117**, 023002 (2016).
- [29] N. Camus, E. Yakaboylu, L. Fechner, M. Klaiber, M. Laux,

- Y. Mi, K. Z. Hatsagortsyan, T. Pfeifer, C. H. Keitel, and R. Moshhammer, Experimental evidence for quantum tunneling time, *Phys. Rev. Lett.* **119**, 023201 (2017).
- [30] U. S. Sainadh, H. Xu, X. Wang, A. Atia-Tul-Noor, W. C. Wallace, N. Douguet, A. Bray, I. Ivanov, K. Bartschat, A. Kheifets, *et al.*, Attosecond angular streaking and tunnelling time in atomic hydrogen, *Nature* **568**, 75 (2019).
- [31] N. Eicke, S. Brennecke, and M. Lein, Attosecond-scale streaking methods for strong-field ionization by tailored fields, *Physical Review Letters* **124**, 043202 (2020).
- [32] I. A. Ivanov and A. S. Kheifets, Strong-field ionization of he by elliptically polarized light in attoclock configuration, *Phys. Rev. A* **89**, 021402 (2014).
- [33] A. S. Landsman and U. Keller, Attosecond science and the tunnelling time problem, *Phys. Rep.* **547**, 1 (2015).
- [34] N. Teeny, E. Yakaboylu, H. Bauke, and C. H. Keitel, Ionization time and exit momentum in strong-field tunnel ionization, *Phys. Rev. Lett.* **116**, 063003 (2016).
- [35] J. Kaushal, F. Morales, L. Torlina, M. Ivanov, and O. Smirnova, Spin-orbit larmor clock for ionization times in one-photon and strong-field regimes, *J. Phys. B* **48**, 234002 (2015).
- [36] N. Eicke and M. Lein, Attoclock with counter-rotating bicircular laser fields, *Phys. Rev. A* **99**, 031402 (2019).
- [37] R. Ramos, D. Spierings, I. Racicot, and A. Steinberg, Measurement of the time spent by a tunnelling atom within the barrier region, *Nature* **583**, 529 (2020).
- [38] C. Meng, W. Chen, X. Wang, Z. Lü, Y. Huang, J. Liu, D. Zhang, Z. Zhao, and J. Yuan, Enhancement of terahertz radiation by using circularly polarized two-color laser fields, *Applied Physics Letters* **109**, 131105 (2016).
- [39] V. A. Tulsy, M. Bagheri, U. Saalmann, and S. V. Popruzhenko, Boosting terahertz-radiation power with two-color circularly polarized midinfrared laser pulses, *Phys. Rev. A* **98**, 053415 (2018).
- [40] C. Tailliez, A. Stathopoulos, S. Skupin, D. Buožius, I. Babushkin, V. Vaičaitis, and L. Bergé, Terahertz pulse generation by two-color laser fields with circular polarization, *arXiv preprint arXiv:2007.08191* (2020).
- [41] G. L. Yudin and M. Y. Ivanov, Nonadiabatic tunnel ionization: Looking inside a laser cycle, *Phys. Rev. A* **64**, 013409 (2001).
- [42] K.-Y. Kim, Generation of coherent terahertz radiation in ultrafast laser-gas interactions, *Physics of Plasmas* **16**, 056706 (2009).
- [43] L. Torlina and O. Smirnova, Time-dependent analytical r-matrix approach for strong-field dynamics. i. one-electron systems, *Phys. Rev. A* **86**, 043408 (2012).
- [44] B. D. Bruner, Z. Mašín, M. Negro, F. Morales, D. Brambila, M. Devetta, D. Faccialà, A. G. Harvey, M. Ivanov, Y. Mairesse, *et al.*, Multidimensional high harmonic spectroscopy of polyatomic molecules: detecting sub-cycle laser-driven hole dynamics upon ionization in strong mid-ir laser fields, *Faraday discussions* **194**, 369 (2016).
- [45] M. Y. Ivanov, M. Spanner, and O. Smirnova, Anatomy of strong field ionization, *Journal of Modern Optics* **52**, 165 (2005).
- [46] M. Hofmann, J. Hyyti, S. Birkholz, M. Bock, S. K. Das, R. Grunwald, M. Hoffmann, T. Nagy, A. Demircan, M. Jupé, D. Ristau, U. Morgner, C. Brée, M. Woerner, T. Elsaesser, and G. Steinmeyer, Noninstantaneous polarization dynamics in dielectric media, *Optica* **2**, 151 (2015).
- [47] A. Sommer, E. M. Bothschafter, S. A. Sato, C. Jakubeit, T. Latka, O. Razskazovskaya, H. Fattahi, M. Jobst, W. Schweinberger, V. Shirvanyan, *et al.*, Attosecond nonlinear polarization and light-matter energy transfer in solids, *Nature* **534**, 86 (2016).
- [48] M. T. Hassan, T. T. Luu, A. Moulet, O. Raskazovskaya, P. Zhokhov, M. Garg, N. Karpowicz, A. M. Zheltikov, V. Pervak, F. Krausz, *et al.*, Optical attosecond pulses and tracking the nonlinear response of bound electrons, *Nature* **530**, 66 (2016).
- [49] F. Morales, T. Bredtmann, and S. Patchkovskii, isurf: a family of infinite-time surface flux methods, *Journal of Physics B: Atomic, Molecular and Optical Physics* **49**, 245001 (2016).
- [50] G. L. Yudin and M. Y. Ivanov, Nonadiabatic tunnel ionization: Looking inside a laser cycle, *Phys. Rev. A* **64**, 013409 (2001).

ACKNOWLEDGMENTS

I.B., A.D. and U.M are thankful to Deutsche Forschungsgemeinschaft (DFG) (projects BA 4156/4-2, MO 850-19/2) as well as Cluster of Excellence PhoenixD (EXC 2122, Project ID 390833453) for financial support. O.G.K., I.A.N., N.A.P., D.E.S. thank the support from Russian Science Foundation, grant Nr. 21-49-00023 and National Natural Science Foundation of China 12061131010. SS acknowledges support by the Qatar National Research Fund (Grant NPRP 12S-0205-190047) and HPC resources from GENCI (Grant # A0080507594). Á.J.G. acknowledges funding from the European Union's Horizon 2020 research and innovation programme under the Marie Skłodowska-Curie grant agreement no. 101028938.

AUTHOR CONTRIBUTIONS

I.B. suggested the idea, developed the quantum Drude-like model, performed simulations and analytics based on this model, performed TDSE simulations; A.J.G performed TDSE simulations for the two-color case; S.S., O.G.K., I.A.N., N.A.P., and D.E.S. performed simulations of unidirectional propagation equations; J.R.C.A, M.K., D.Z., L.S. and V.V., performed the experiment; I.B., A.J.G, A.H., F.M., L.B., S.S., U.M., A.D., T.N., M.V. and M.I. analyzed and interpreted the results of the simulations and experiments; all authors participated in the article formulation and writing.